UC Berkeley
UC Berkeley Previously Published Works

Title

Seasonality of Retreat Rate of a Wave-Exposed Marsh Edge

Permalink

Journal

ISSN

Authors

WinklerPrins, Lukas

Lacy, Jessica R

Stacey, Mark T

et al.

Publication Date

DOI

Copyright Information

Correspondence to:

L. WinklerPrins,
lukas_wp@berkeley.edu

Seasonality of Retreat Rate of a Wave-Exposed Marsh Edge

Lukas WinklerPrins[1,2] , Jessica R. Lacy[1] , Mark T. Stacey[2] , Joshua B. Logan[1] , and Andrew W. Stevens[1]

[1]U.S. Geological Survey, Pacific Coastal and Marine Science Center, Santa Cruz, CA, USA, [2]Civil & Environmental Engineering, University of California, Berkeley, CA, USA

Abstract Wave-driven erosion of marsh boundaries is a major cause of marsh loss, but little research has captured the effect of seasonal differences on marsh-edge retreat rates to illuminate temporal patterns of when the majority of this erosion is occurring. Using five surface models captured over a study year of a marsh with a steep escarped boundary in South San Francisco Bay, we find a pronounced seasonal signal, where rapid marsh retreat in the spring and summer is driven by a strong sea breeze but little change is found in the marsh-edge position in the fall and winter. We found accretion in the mudflat transition region close to the marsh boundary in the calmer seasons however, suggesting intertwined morphodynamics of mudflats and the eroding marsh-scarp. We observed large spatial heterogeneity in retreat rates within seasons, but less on longer (annual and decadal) timescales. The relationship between marsh-edge retreat rates and properties of the wave field nearby is explored and contextualized against extant relationships, but our results speak to the difficulty in addressing spatial erosion/accretion variability on short (seasonal) timescales with simple models.

Plain Language Summary Waves can cause destruction of marshlands when they collide with the boundary of the marsh area. We studied how the speed of marsh loss from waves can change between seasons with different climates. To do this we made five 3D models of a marsh in South San Francisco Bay over a single year and looked at their differences between summer/fall/winter/spring. We found fast marsh loss in the seasons where daily winds are common (spring/summer), and minor changes in seasons with storms but without daily winds (fall/winter). Across our entire marsh, we saw lots of variety in how much it was changing, including some addition (i.e., positive change) to the mudflats near the marsh in the fall/winter. When we compared the marsh loss over one year to what was lost between 2004 and 2019, the speeds were similar, so we believe our study period was similar to long-term marsh dynamics. This work encourages incorporating different seasonal climates into expectations of how marshes evolve, and supports that we need to think about marshes and mudflats as connected in how they change over time.

1. Introduction

Marsh ecosystems are valuable for the myriad services they provide, including critical habitat for threatened and endangered species, coastal protection, and carbon sequestration. Marshes globally are losing extent due to coastal erosion (Campbell et al., 2022), endangering these benefits and exacerbating "coastal squeeze" between erosion and the built environment along developed coastlines (Torio & Chmura, 2013).

In San Francisco Bay, a heavily urbanized coastal region, diking and filling eliminated more than 90% of extant marshlands following European colonization (Williams & Faber, 2001), with those remaining imminently threatened by erosion or drowning (K. Thorne et al., 2018). Lateral retreat rates of −0.5 m/yr from central San Francisco Bay have been reported from recent years and retreat rates of −1 m/yr or more in time periods from earlier in the 20th century (Carkin et al., 2020). Beagle et al. (2015) found mostly expanding marsh edges in San Pablo Bay (north San Francisco Bay), and only a portion of one marsh in this region was found to be retreating nearly −2 m/yr (R_L) between 1993 and 2010. This study begins to quantify loss of marsh lands in South San Francisco Bay (SSFB).

Lateral erosion of marsh-edge boundaries caused by the impact of incident water surface waves is a major process contributing to coastal marsh loss (Leonardi, Ganju, & Fagherazzi, 2016; Mel et al., 2022). Dimensional analysis (Marani et al., 2011) and empirical studies (Bendoni et al., 2016; Leonardi, Ganju, & Fagherazzi, 2016; McLoughlin et al., 2015; Mel et al., 2022) suggest a linear relationship between incident surface wave power and annualized volumetric erosion rates at the marsh edge. However, nonlinear relationships have been observed as well (Cadigan et al., 2023; Houttuijn Bloemendaal et al., 2023), and Houttuijn Bloemendaal et al. (2023) revisited

the assumption of linearity in this relationship, noting that once marsh-edge retreat and wave power distributions are log-transformed into normal distributions, some marsh systems exhibited power-law relationships. Marsh-edge retreat may happen in sudden moments of mass such as slump-block or cantilever failure, delayed after wave impact (Bendoni et al., 2016; Cadigan et al., 2023). Because of this time-lagged effect, the time period duration between marsh-edge location observations affects the extent of inclusion of failure events, which could be a critical factor in the observed wave power-retreat relationship, as was found in Mel et al. (2022); Bendoni et al. (2016). While the extant body of research points toward a multitude of site- and mechanism-specific factors that lead each individual marsh system to have a unique wave power-retreat relationship, many studies have focused on yearly or multi-year timescales (Leonardi & Fagherazzi, 2015; Marani et al., 2011; Schwimmer, 2001), and intra-site variability of retreat has rarely been explored. Thus, prior studies have yet to identify seasonal patterns in marsh-edge morphodynamics, despite implied seasonality following seasonal patterns in wind and wave forcing. Some studies have captured marsh-edge failure and retreat on timescales shorter than months (Cadigan et al., 2023; McLoughlin et al., 2015), but none have drawn attention to seasonal climatic patterns that may affect marsh morphodynamics. Recent advances to capture and process high-resolution aerial photogrammetry (<0.3 m pixel), make data collection of marsh environments possible at small spatiotemporal scales (Gray et al., 2018; Pinton et al., 2020), enabling study of marsh-edge morphodynamics beyond just the movement of the marsh-edge boundary.

In this study, we explored marsh-edge retreat over four seasons of a study year (May 2021–May 2022) using five high-resolution digital surface models (DSMs) derived from structure-from-motion (SfM) photogrammetry, and modeled wave conditions for each season between site surveys. We added context to this 4-season (summer, fall, winter, spring) comparison with recent decadal-scale retreat rates at the site established using lidar data sets from 2004, 2010, and 2019. Within and across seasons, we used our DSMs to quantify the spatial heterogeneity and temporal variation in marsh-edge retreat. We found evidence of a difference in morphodynamics between spring/summer and fall/winter, which followed the regional wind and wave seasonality. We placed our study year in the context of recent decades of wind history and marsh loss for the region. Lastly, we explored the relative merits of our elevation-based marsh-edge boundary delineation and comparison of our site's wave power-retreat rate relationship to those in the literature.

2. Study Site

Our field site was Whale's Tail Marsh South (WTMS), a small (0.71 km^2) marsh with significant anthropogenic influence due to land use change and nearby development in SSFB, California. WTMS is along the south-eastern edge of SSFB, so the marsh's western edge (orange in Figure 1a) is exposed to a long in-bay fetch with prevailing northwesterly winds, as can be seen in Figure 1b—approximately 30 km along a line of 320° heading. The marsh edge—the boundary between high marsh and unvegetated mudflat—has a nearly north-south orientation of approximately 350°. The marsh-top platform is covered in a dense vegetated mat of pickleweed, marsh gum plant, and occasional other species, but is virtually unvegetated within 1–2 m of the edge close to the bay (Figure 1c). The bayside edge of the marsh at WTMS is characterized by a steep escarpment or "scarp," typically between 0.3 and 2 m tall, with a grade of 60% or more, separating mudflats from high marsh. The marsh is disconnected from any terrestrial flow. Tides in San Francisco Bay are mixed semidiurnal. As measured at the NOAA Redwood City station, on the western side of SSFB (as in Figure 1b), mean higher-high water is at 2.14 m and mean lower-low water at −0.36 m relative to the NAVD88 datum.

WTMS is enclosed within SSFB, and protected from open-ocean conditions by the San Francisco Peninsula to the west. The mouth of the bay is nearly 39 km away, and while ocean-originating swell waves have been observed inside San Francisco Bay in Talke and Stacey (2003), those observations were much closer to the mouth and with a more direct path for the swell; we expect all waves at the study site to be generated by in-bay winds. During the spring and summer months, there is typically a daily sea breeze which begins in late morning and abates in late afternoon or early evening (Conomos et al., 1985). There are intermittent winter storms in SSFB, with those in our study period coming from the S-SW.

The site and its context in SSFB are heavily impacted by development and restoration. To the east and south of WTMS are levees that separate the marsh from former salt harvesting ponds which are in the process of restoration to marshlands as part of the South Bay Salt Pond Restoration Project. The northern boundary is a levee that
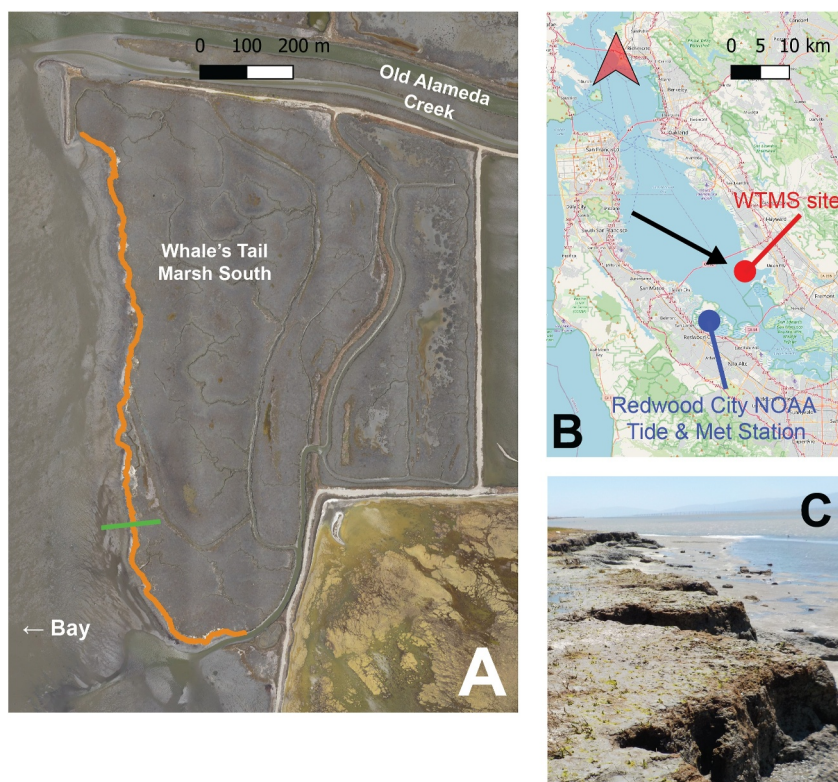
Figure 1. (a) Aerial orthomosaic photo of Whale's Tail Marsh south (WTMS) in May 2022 with marsh-edge boundary drawn in orange at elevation of the scarp head contour. The green line is the location of an example cross-sectional transect (shown in Figure 2), but is artificially lengthened for legibility. (b) Map of South San Francisco Bay, with red indicating the location of WTMS and blue indicating location of the NOAA Redwood City Tide Gauge and Met Station. The black arrow is aligned with the most common wind direction during spring and summer seasons. (c) Photograph from atop the marsh surface on 19 May 2021 11:58 a.m. PDT, showing the relationship between high-marsh platform, steep scarp edge, crenulated coastline, and fronting mudflats. The photo was taken approximately 50 m south of the green transect in panel (a), facing southwards. Photo by J. R. Lacy, U.S. Geological Survey.

separates marsh from the flood control channel called "Old Alameda Creek," the former outfall of Alameda Creek (Stanford et al., 2013).

3. Methods

3.1. Imagery Collection and Digital Surface Model

Aerial images of WTMS were collected by air, flying at approximately 427 m above ground level on five dates: 30 May 2021, 9 September 2021, 14 November 2021, 10 February 2022, and 19 May 2022, thus bracketing four seasons (May–September as 102-day "summer," September–November as 66-day "fall," November–February as 88-day "winter," and February–May as 99-day "spring"), and 355 days in total (which we will refer to as our "study year"). Flights were timed to coincide with lower-low tides that occurred close to solar noon for best exposure of the marsh edge. The imagery were used to derive 5 cm-resolution digital surface models (DSMs) using structure-from-motion (SfM) processing techniques described in Over et al. (2021), with survey control established using 20 ground control points surveyed with survey-grade post-processed kinematic GNSS. DSMs and RGB orthomosaic images are available in Logan et al. (2023). We used three pre-existing digital elevation models from lidar data sets: two collected May 2004 (Foxgrover & Jaffe, 2005) and November 2010 (OCM Partners, 2023) from the USGS in 1 and 2 m resolution respectively, and one from between July and August 2019 from Alameda Creek Flood Control and Water Conservation District in 0.914 m (3 feet) resolution (Winkler-Prins, 2023). Due to the multi-day acquisition for the lidar data, we assigned an approximate date to these data for the purpose of calculating retreat rates: the 15th day of the known survey month (for 2004 and 2010) and the middle day of the provided range (thus July 24th, for 2019). Due to the long duration of the decadal study used for
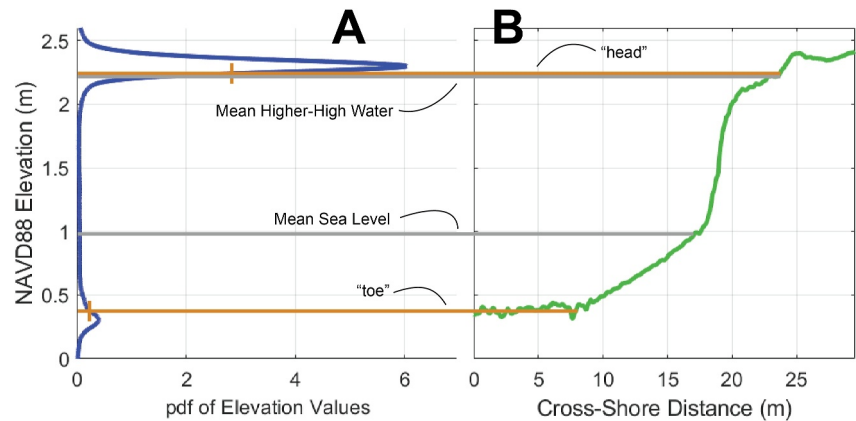
Figure 2. (a) Schematic of how toe and head elevations were determined by the distribution of elevations in a given digital surface model, with elevations that intersect points at the half-prominence of each peak in the distribution. These elevations are mapped on to an example marsh-edge elevation transect in panel (b), as indicated in green in Figure 1. The region between the toe and head intersections is analyzed for volumetric erosion.

the 2004, 2010, and 2019 data sets, the possible error introduced by this approximation is <2% of the calculated retreat rates.

The DSMs generally represent the top of the vegetation canopy rather than bare earth. The marsh-top surfaces in the DSMs are at approximately 2.4 m (NAVD88). Using RTK GNSS data collected by walking the marsh surface in southern WTMS on 1 December 2021, we found a mean 0.22 m offset between the DSM surface and ground surface, consistent with vegetation offsets found in San Francisco Bay by Buffington et al. (2016), and suggesting that the bare-earth marsh platform is at around 2.2 m (NAVD88). Because our technique for marsh-edge delineation (Section 3.2) is not vegetation-based but rather from hypsometry of the entire region, we believe the vegetation offset does not affect our observed retreat rates. This is aided by the fact that several meters of the seaward portion of the marsh-top platform at WTMS is mostly unvegetated and sits at an elevation of approximately 2.18 m (NAVD88). The high marsh platform is only inundated at high tides, and often only during spring tide cycles. Offshore of the marsh region, below the scarp, is more than a kilometer of intertidal mudflats, generally below 0.4 m (NAVD88). Further details about precision and accuracy of the DSMs are described in Section 3.3.

3.2. Marsh Edge Delineation

In order to delineate the region of the eroding marsh edge, we sought to find elevations representative of the "toe" (lower elevation) and "head" (upper elevation) of the mudflat-to-marsh transition zone which includes the scarp. DSMs were clipped to regions including only the marsh-top surface of WTMS and 30–70m of the fronting mudflats, extending out to where noise-free data were collected during the photogrammetry process (i.e., dry regions of the mudflats). For each of these trimmed DSMs—the five from SfM processing, and 3 from lidar—we generated probability density distributions representing the distribution of NAVD88 elevation values at each pixel, as in panel A of Figure 2. Due to the characteristic presence of a relatively sharp scarp at WTMS, each distribution contained two clearly separated peaks: the smaller, lower-elevation peak representative of the fronting mudflats and bottom surface of channels within the marsh; and the larger, higher-elevation peak representative of the top-of-vegetation surface. At the lower-elevation peak, we defined the higher-elevation half-prominence elevation as the toe elevation, an upper bound on the elevations of mudflats. At the higher-elevation peak, we defined the lower-elevation half-prominence elevation as the head elevation of the scarp a lower bound on the elevations of the marsh-top platform and vegetation (Figure 2). We performed this process eight times to get a toe elevation and head elevation for each DSM. We used the region between the head and toe elevation contours as the marsh-edge transition area for each survey. Head contour elevation values ranged from 2.179 to 2.267 m (NAVD88), and we used the lowest-elevation value (i.e. 2.179 m) in *all* DSMs as the marsh-edge boundary in our linear retreat analysis (see Section 3.4) to stay consistent with shoreline retreat analyses which generally use a single fixed elevation. Toe elevations ranged between 0.363 and 0.384 m (NAVD88), and we use 1.8 m as a normative distance between the toe and head—a scarp height.

Table 1
Positional Uncertainties of the Five Digital Surface Models Collected Over Our Study Year and of the Three Pre-Existing Lidar Data Sets

Uncertainties (m)	05/2004	11/2010	07/2019	05/2021	09/2021	11/2021	02/2022	05/2022
Total Horiz. Unc.	1.2	2.0	1.4	0.079	0.086	0.096	0.082	0.086
Total Vert. Unc.	0.25	0.03	0.60	0.063	0.103	0.040	0.042	0.042

Note. Note the horizontal uncertainty values include "resolution error," from the pixel size, whereas vertical do not.

3.3. Spatial Accuracy

Determining spatial accuracy or uncertainty grants us confidence in our observed marsh retreat metrics. Each SfM-derived DSM had satellite-derived horizontal and vertical positional uncertainties as determined by comparisons against a number of ground control points across the study site, with details explained in Logan et al. (2023). A combination of RMSE horizontal position discrepancies based on ground control points in each DSM and an estimated 0.020 m GNSS ground control error, included by summation in quadrature, gave a total alignment positional horizontal uncertainty of each DSM. A similar procedure was followed for vertical uncertainty, with an estimated 0.030 m ground control error. For the purposes of accurately drawing the location of the marsh-edge boundary curve in the horizontal plane, we also included the pixel size in quadrature as a "resolution error," for a combined horizontal plane location uncertainty value. Total positional uncertainty values are presented in Table 1. Note that these uncertainties are averages from the ground control points and that uncertainties may vary spatially in the DSMs.

The lidar data sets from 2004, 2010, and 2019 had reported pixel resolutions of 1, 2, and 0.914 (3 ft) meters respectively. The 2004 lidar data have horizontal accuracies of 20–60 cm and vertical accuracies of 15–25 cm (Foxgrover & Jaffe, 2005), and the 2010 "better than 2 cm horizontal and 3 cm vertical" but accuracies are unknown for the 2019 data set. Using the upper value estimates of uncertainty from the 2004 and 2010 data sets, in addition to 1 m horizontal and 0.6 m vertical (conservatively) for the 2019 data set as estimate leads to combined uncertainty metrics in Table 1. The horizontal plane uncertainty metrics also include resolution error.

3.4. Marsh Retreat Statistics

Marsh retreat was calculated in two characteristically different ways. The first method was shoreline movement analysis, where the distances between shoreline curves—using the fixed marsh head elevation curves described in Section 3.2—were calculated to determine annualized linear retreat rates of the marsh-edge curves, R_L, in m/yr. To do this, we used the Digital Shoreline Analysis System (DSAS) v5.1 (Himmelstoss et al., 2021) in ESRI ArcMAP v10.8.2, a package that has been used for coastal marsh retreat analysis previously in SSFB (Carkin et al., 2020) and in Virginia (McLoughlin et al., 2015). In DSAS, we used an eastward-shifted and generalized version of the 2022 marsh head curve as a baseline curve. From this curve, 1,265 perpendicular transects at 1 m spacing were drawn. Linear rates of retreat (R_L) were calculated at each transect by dividing the distance between the transect-curve intersections and the interval, in years, between the shoreline curves. To convert R_L values to a per-unit-width volumetric marsh loss values (in m^3/m/yr) for comparison with prior studies, we multiplied by the normative scarp height h, approximately 1.8 m.

Small crenulations in the marsh-edge curve, non-perpendicular intersections between transects and marsh-edge curves, and mass failure of thin marsh features separate (e.g., marsh "necks," using language from Schwimmer (2001)) led to dramatically high R_L values at a small number of specific transects. We thus removed outlier R_L values with absolute values greater than 20 m/yr in our analysis (at most, 1.9% of total transects from a given time interval). Furthermore, we present median statistics to account for some bias of unrealistically extreme R_L values stemming from these problems in the transect-based technique. Some portions of the marsh registered bayward expansion between data sets, especially in the Fall season. Given a lack of explanatory mechanism for bayward growth of a scarp-shaped interface, these values required investigation, further addressed in Sections 4.2 and 5.2. Despite this complication, we present metrics inclusive of positive (i.e., progradational) R_L values, but with outliers removed. When we ran a spatially lagged autocorrelation function to determine an effective number of independent transects (as done by DSAS per Ruggiero et al. (2013)), we found that no two transects were

Table 2
Marsh Retreat Metrics per Unit Width: Linear Retreat R_L, Volume Loss by DSM of Difference $R_{V,DoD}$, and Volume Loss by Transect $R_{V,tsect}$

Per-width retreat rates	2004–2019	2021–2022 years	Summer	Fall	Winter	Spring
Median R_L (m/yr)	-1.69 ± 0.34	-1.46 ± 0.12	-2.49 ± 0.42	$+0.12 \pm 0.71$	-0.28 ± 0.52	-2.25 ± 0.44
$R_{V,\text{DoD}}$ (m³/m/yr)	-4.18 ± 0.28	-3.78 ± 0.25	-7.92 ± 3.247	$+2.33 \pm 3.078$	$+0.47 \pm 0.69$	-8.00 ± 0.86
Median $R_{V,\text{tsect}}$ (m³/m/yr)	-3.98	-3.60	-7.68	$+1.47$	$+0.07$	-7.12
Mean Wave Power (W/m)	n/a	54.9	87.0	41.1	6.2	80.0

Note. Uncertainties in R_L are combinations of positional uncertainties of the marsh-edge curves (Table 1); uncertainties in $R_{V,\text{DoD}}$ are from systematic, uncorrelated, and spatially correlated errors in the DoDs, described in Section 3.4.

independent. As such, the uncertainties presented on R_L in Table 2 are the uncertainties of the shoreline positions from Section 3.3, summed in quadrature and annualized.

The second method to quantify marsh retreat consisted of subtracting DSMs from one another to calculate volume change between survey dates (commonly denoted R_V). This was thus inclusive of all change between survey dates, capturing any volumetric accretion as well—although we will typically call it a retreat rate. To do this, we drew polygons between the head and toe elevation contours of the two DSMs of interest in order to calculate elevation difference only in the unvegetated marsh-edge region. Within this polygon, we subtracted the earlier DSM from the latter DSM to find a DSM of difference (DoD). This DoD was then summed to find the volume change between the surfaces, ΔV_{DoD}. We then found the average volumetric change rate (per unit width) by dividing by the time interval and a representative marsh-edge length L (1,109 m). Thus we calculated a marsh-representative volumetric change (or retreat) rate $R_{V,\text{DoD}} = \Delta V_{\text{DoD}}/(\Delta t * L)$ (m³/m/yr). While this technique was explanatory for total-system volumetric change, it neglected to quantify the loss of blocks from the edge of the marsh platform that remained local (as the total volume of marsh material in the region would not change).

In order to investigate volumetric retreat on a per-transect basis for spatial analysis, we used a similar technique, differencing 2D elevation profiles extracted from the DSMs between toe and head elevations along the transects drawn by DSAS. The difference between these drawn elevation transects represented a per-unit volumetric loss, which we term $R_{V,\text{tsect}}$ (also in m³/m/yr). We omit discussion of variability in R_L (due to spatial heterogeneity) in favor of using this volumetric $R_{V,\text{tsect}}$ metric. The distributions of transect-level volumetric retreat rate values ($R_{V,\text{tsect}}$) due to spatial variability across the marsh are presented in Section 4.2 and explored in Section 5.2.

The uncertainty values on $R_{V,\text{DoD}}$ are the annualized summed-in-quadrature uncertainties of random errors, spatially correlated errors, and systematic errors in the DoDs, ala equation 21 in Anderson (2019). Because of the large amount of geomorphic change near the marsh-scarp, these numbers are populated from stable regions elsewhere in the DoDs. Portions of unvegetated levee-top regions ($\sim$25 m diameter) were used to quantify systematic and random errors. The spatially correlated error was found via the process of Anderson (2019); Rolstad et al. (2009). To effectively resolve the semivariogram, we used a larger region ($\sim$200 m diameter) in the interior of the marsh with negligible geomorphic change. This was likely to overestimate error due to the presence of vegetation although phenological change of pickleweed is minor. We found the best-fit variogram for all surveys to be an exponential model with range of 6 and zero nugget. The sill of each semivariogram ($\sigma_{\delta z}$ in the notation of Rolstad et al. (2009)) was transformed into an uncertainty by integration of the exponential semi-variogram model and scaling by marsh length and time interval. We neglect to present uncertainty values on the $R_{V,\text{tsect}}$ values due to the complex process for their calculation; however, their uncertainties should reflect those of $R_{V,\text{DoD}}$ as they sample the same DoDs.

3.5. Wave Observations and Model

We collected in situ wave data using downward-facing acoustic Doppler velocimeters installed subtidally during the summer and winter study periods to support this study (Ferreira et al., 2023). The platform was located approximately 2.23 km from the scarp in the summer, and 1.90 km in the winter (distances perpendicular from the boundary of the central marsh). Data were collected at 8 Hz for 260 s every 15 min and we used spectral techniques to find H_{m0} (as H_S, significant wave height) and T_p (peak wave period) for each burst, following Madsen (1995) and Wiberg and Sherwood (2008).
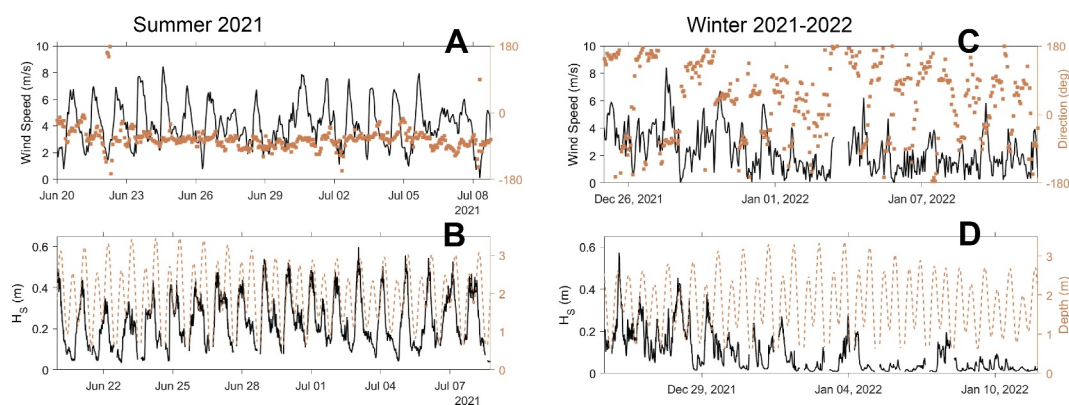
Figure 3. Eighteen days of timeseries data from the summer (a), (b) and winter (c), (d) seasons. Wind data were taken from the Hayward, CA station of the model in King (2019), the closest to our field site. Summer is dominated by 2–6 m/s diurnal winds from the northwest, whereas in the winter we see the taper of storm conditions into calmer conditions, with highly variable wind direction. Wave heights follow associated patterns in wind speeds.

To generate wave-field data over our entire study year, we applied a SWAN spectral wave model of SSFB. We used a Collins (1972) bottom friction parameterization (value 0.02), whitecapping formulation from Van Der Westhuysen et al. (2007), and a Battjes and Janssen (1978) depth-induced breaking model on a nested grid (81×172 with approximately 300 m resolution). We ran the wave model using hourly 3 km-resolution wind input from NOAA's High-Resolution Rapid Refresh. We extracted wave metrics from the model at the site of observed wave conditions, about 6 grid cells from the marsh boundary.

We validated the model by comparison against observed spectral wave metrics in the summer (7 June–11 August 2021) and winter (23 November 2021–31 January 2022) seasons. In the summer, the model recreated the daily sea breeze-driven wave field. For the summer season, RMSE of H_S was 0.08 m against a modeled seasonal-mean H_S of 0.22 m. In the winter, RMSE was 0.07 m against a modeled seasonal-mean H_S of 0.10 m. Some of the proportionally high RMSE value is due to temporal mismatch of peaks in H_S values rather than mis-estimation in total. These comparisons generally indicated slight over-estimation of wave heights by the model. This was most prominent during winter-season storms. However, given sufficient agreement to capture seasonal differences, we used model output to populate wave power metrics in all four seasons for our analysis. Further details of this wave model are available in WinklerPrins and Stevens (2024).

Incident wave power was calculated as:

$$P_w = \frac{c_g \rho g H_S^2}{8} \cos(\alpha) \tag{1}$$

where c_g is the wave group celerity, ρ is water density, g is the force of gravity, H_S is the significant wave height, and α is the angle between the average marsh-bay interface normal direction (260°) and the incident wave direction. We calculated seasonally representative P_W values by averaging burst-mean P_W values over each season, including only data from periods of time when the burst-mean water surface elevation was between the elevations of the scarp toe and head.

For comparison of wind conditions in our study year versus longer-term norms of SSFB, we used data collected at NOAA station 9414523 in Redwood City (visible in panel B of Figure 1), which had a long-term wind record.

4. Results

4.1. Wave Conditions

Waves were typical of in-bay conditions during our study year. During warm-season days, the onshore sea breeze (Figure 3a) typically produced H_S values of 20–35 cm each day which typically peaked around 15:00 local time in the afternoons (Figure 3b). Modeled wind conditions at a Hayward, CA station slightly inland of WTMS, from King (2019), were typically from the W to NNW with peak wind speeds over 6 m/s. In the fall and winter,
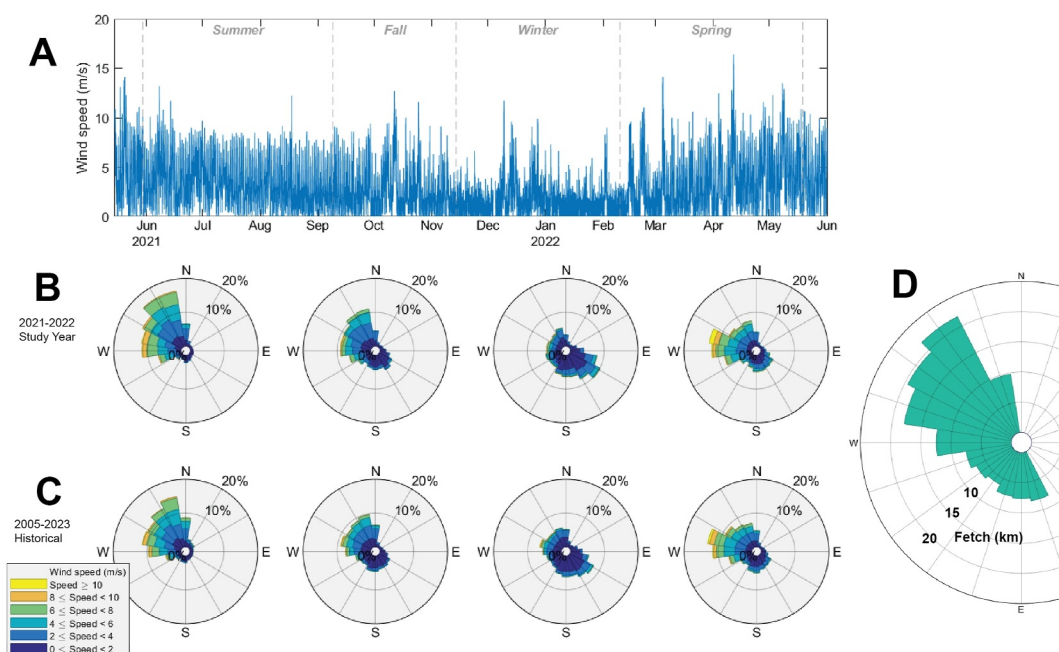
**Figure 4.** (a) Timeseries of wind speeds over our study year, as measured at the Redwood City NOAA Station. (b) Wind roses of the same data from the four seasons in our study year (summer/fall/winter/spring left-to-right). (c) Wind roses of historical wind conditions from 2005 to 2023, split up between the seasonal ranges from our study year (same order). (d) Rose of fetch distances over San Francisco Bay from Whale's Tail Marsh, capturing the long fetches to the northwest.

conditions were generally calm with variable but often southwesterly winds (Figure 3c), punctuated by storm events with wind speeds over 6 m/s and H_S over 40 cm (Figure 3d). Storm winds were highly variable in direction but tended to be between SSE-SW. Winds from the SE did not contribute to the wave field at our field site due to no fetch in that direction (Figure 4d). Despite similar peak wind speeds, sea breeze winds generally came from directions with longer fetch distances and produced slightly larger waves. In all seasons, maximum wave heights were affected by tidal depth, with the largest H_S values occurring during simultaneous high water depths and high wind conditions, as expected in a shallow enclosed bay (Foster-Martinez et al., 2018; WinklerPrins et al., 2023). Most winter storm events were long enough to persist over one or more tidal cycles. During warm seasons with sea breezes, the timing of afternoon winds and waves with tidal depth peaks shifted over time, sometimes aligning and sometimes not. Model outputs suggested no variation in wave conditions across the length of WTMS at the bay interface.

Our study year had only approximately five storm events over the fall and winter seasons, and two in late February/early March, included in our spring study period. Wind roses as measured at Redwood City in SSFB of our study year (Figure 4b) broadly agreed with decadal-scale averages (2006–2023) (Figure 4c), suggesting our year was relatively "typical" despite California's dynamic climate.

4.2. Marsh-Edge Retreat Rates

Marsh-edge retreat rates varied strongly by season and were correlated with mean wave power. Median annualized volumetric erosion rates $R_{V,\text{DoD}}$ were rapid, ~-8 m³/m/yr in the spring and summer seasons, with negligible change or potential accretion observed in the fall and winter (Table 2). While the summer-season $R_{V,\text{DoD}}$ uncertainty was higher than other seasons, so was the retreat rate. The uncertainties in $R_{V,\text{DoD}}$ values for the fall and winter seasons made their marsh-wide $R_{V,\text{DoD}}$ rates indistinguishable from zero. Linear retreat analysis via R_L produced a similar pattern, with rapid (<−2 m/yr) retreat of the marsh scarp in the spring/summer and negligible change in the fall and winter seasons. The level of uncertainty in R_L metrics in the fall and winter suggests little change in shoreline position during those seasons. Close inspection of the DoDs revealed likely accretion over the mudflats just offshore of the marsh scarp in the fall and winter, reflected in the $R_{V,\text{DoD}}$ values. These patterns are further discussed in Section 5.2. Representative $R_{V,\text{tsect}}$ values broadly agreed with $R_{V,\text{DoD}}$ values, although the
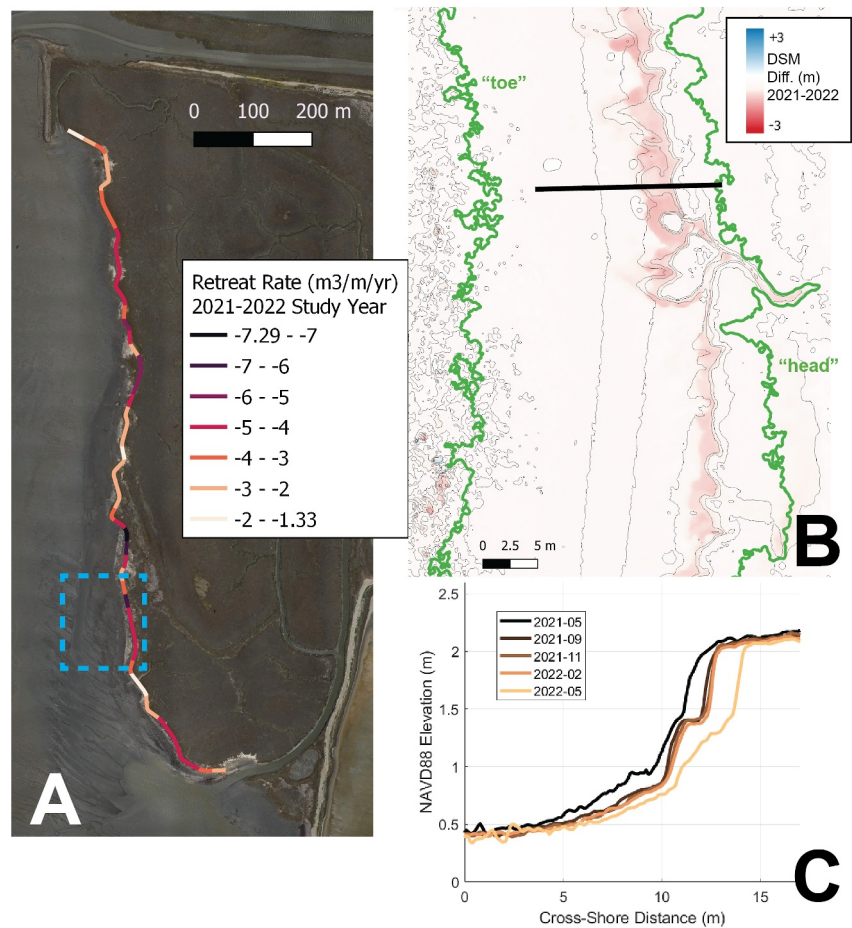
Figure 5. (a) The marsh-edge curve broken into 55 segments, colored by average study-year transect-level volumetric retreat rate ($R_{V,\text{tsect}}$) values in each segment. The blue dashed rectangle represents the region captured in panel (b), which shows a blue-red map of elevation difference values (in meters) between May 2021 and May 2022 surveys. The contours are spaced at 0.3 m intervals of the May 2022 DSM, and the green curves are the associated toe (left) and head (right) elevation contours, bounding the region of the DoD. (c) Displays elevation transects over the five study-year surveys along the line drawn in black in panel (b) as an example of landward retreat of the marsh-scarp edge.

former tended to be smaller in magnitude, and this gap was greatest in the fall and winter seasons. We attribute the discrepancy between the values to the irregular sub-sampling of the DSM inherent in the $R_{V,\text{tsect}}$ technique. Transects drawn perpendicular to the marsh-edge head curve undersampled the mudflat transition region because the marsh-edge head curve is typically gently convex toward the bay. This undersampling of the mudflat transition zone would lead $R_{V,\text{tsect}}$ to slightly underestimate in magnitude the actual total-marsh change presented by $R_{V,\text{DoD}}$.

Transect retreat rates ($R_{V,\text{tsect}}$) varied across the length of the marsh boundary as visualized for the study year in Figure 5a. We found no systematic spatial organization of the variation in any season. Seasonal patterns in volumetric change are evident in transect profiles over time, as portrayed in Figure 5c.

The spatial variability in $R_{V,\text{tsect}}$ values across WTMS were also reflected by the cumulative distribution functions (cdfs) in Figure 6. Despite generally narrow distributions, long tails (i.e., very large values of change) led to standard deviation values that were somewhat large compared to median values: standard deviations of $R_{V,\text{tsect}}$ were 1.14, 1.58, 4.34, 4.50, 2.59, and 4.29 m³/m/yr for the decadal analysis, study year, summer, fall, winter, and spring, respectively. The largest-magnitude retreat rates of these tails must be regarded critically given the effects of small features—both real and products of processing—in the high-resolution DSMs and the scaling up to annual retreat rates. These two effects were likely less impactful over the decadal-duration analysis, due to lower-resolution lidar data and the longer timespan. The cdfs of decadal and study-year retreat values agreed well, with
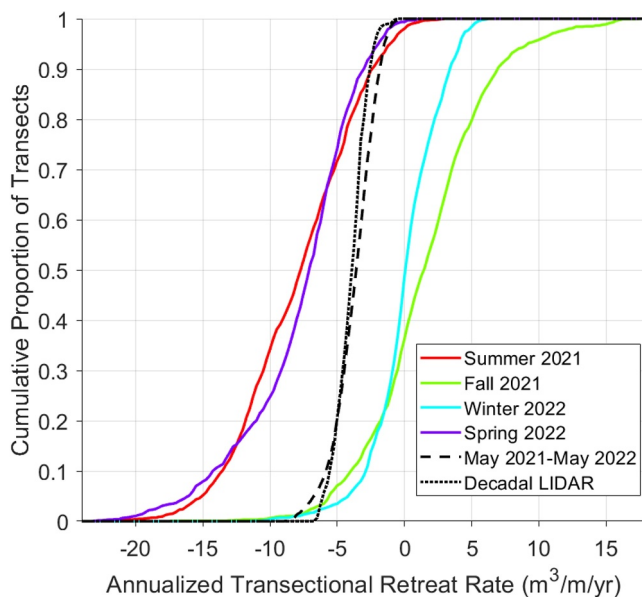
Figure 6. Cumulative distribution functions of transect-by-transect volumetric retreat rate values ($R_{V,\text{tsect}}$, in m³/m/yr) across the marsh, for different time periods.

smaller ranges than the seasonal distributions. The decadal cdf exhibited less tail behavior (excess kurtosis of −0.27) than the study year (excess kurtosis of 0.13). The spring/summer cdfs sat on the erosive side of the longer-term (annual/decadal) distributions, whereas the fall/winter cdfs were more positive. Only the fall season distribution of $R_{V,\text{tsect}}$ values actually had a positive skew, attributable to its transects of high volumetric accretion values, addressed in Section 5.2; the other distributions all had negative skew. The winter season distribution was balanced by both accretional and erosional transects and had the narrowest spread of the seasonal cdfs. In contrast, the spring/summer seasons were dominated by negative $R_{V,\text{tsect}}$ values (i.e., retreat) with somewhat wider spreads in values.

The total volume change (ΔV_{DoD}, used to populate $R_{V,\text{DoD}}$) over the study year was −4,072 m³. Between the four seasons, the volume changes were −2,454 m³, +468 m³, +125 m³, and −1,355 m³ by summer, fall, winter, and spring, respectively. Subsampling of the transition regions inclusive of the mudflats and exclusive of the marsh scarp itself suggested that ≥95% of the total volumetric accretion in the fall and winter seasons can be attributed to accretion in the near-marsh mudflats. Using a representative bulk density of 0.60 g/cm³—the average of marsh-scarp samples taken in K. M. Thorne and Bristow (2023)—and the total loss of sediment over our study year, 4,072 m³, yields the loss of 2.5∗10⁶ kg of sediment from the marsh edge over a year (Note that this bulk density is higher than the 0.40 g/cm³ published in Callaway et al. (2012) at the high marsh, however, that study had only one sample and represents a different region of the marsh system).

5. Discussion

5.1. Seasonality of Marsh-Edge Retreat

Our study quantifies a strongly seasonal variation in marsh-edge retreat, with rapid retreat during the spring and summer seasons with daily sea breeze and little marsh-edge change during the fall and winter when storms occur. This sits in contrast to hurricane-dominated systems which have their associated season but where marsh-edge movement may be dominated by individual events rather than quotidian dynamics. Agreement between retreat rates observed in our study year and over the prior decades—both linear and volumetric—suggests that annual-scale aggregation was appropriate to identify long-term trends, a point also identified by Priestas et al. (2015), and our study year as compared to long wind histories in SSFB suggest our study year was fairly representative (Figure 4). That said, winter storm conditions in coastal California are highly variable (Swain et al., 2018); while the dry-summer wet-winter seasonality is not largely shifting, the intensity of individual winter seasons is subject to large change. Linear retreat analysis (R_L), which used movement of a fixed elevation curve to quantify retreat, showed virtually pure erosion, which is to be expected as a steep scarp has no mechanism for progradation. The positive values and large uncertainties in the volumetric change analysis (via $R_{V,\text{DoD}}$ and $R_{V,\text{tsect}}$) suggested accretion in the region between toe and head elevations. The sediment contributing to accretion may be derived from the eroding marsh-scarp edge; this is further addressed in later sections.

We found that seasons with higher average wave power had larger spreads of marsh-edge retreat rates ($R_{V,\text{tsect}}$) across our study system (Figure 6). However, the ranges of transect-level $R_{V,\text{tsect}}$ values in the study year and decadal analysis were smaller than in any individual season, with the distribution becoming tighter and with thinner tails as timescales got longer. Priestas et al. (2015) suggests that as the average retreat rate increases, the distribution of retreat rate values becomes more normally distributed, whereas in regions or time periods with low average retreat rates, the distribution becomes more asymmetric with a tail of large values away from the origin (i.e., log-normal). We did not observe this pattern exactly in our analyses, but we did find evidence for marsh-wide retreat rates becoming more uniformly distributed and with fewer extreme values given longer intervals of study (also as can be read from Figure 6). This may be because this is a system with high enough wave power to effectively erode protrusions from the marsh edge; put another way, a strong uniform wave field effectively overpowers heterogeneity in marsh-edge erodibility to produce a uniformly eroding marsh boundary on a

sufficiently long timescale (Leonardi & Fagherazzi, 2014; Priestas et al., 2015). Mel et al. (2022) found that inclusion of mass-failure events (rather than only gradual erosion processes) lowered R^2 values of wave power-edge erosion regressions at the monthly scale but increased R^2 values at the annual scale, speaking to how sufficiently long time periods between retreat measurement can effectively aggregate seemingly stochastic mass-failure processes or time-lagged cumulative wave power effects on edge failure (as found on the weekly scale by Cadigan et al. (2023)). Our findings support that seasons can be effective sub-annual timescales for marsh failure observation aggregation, in contexts where seasons drive shifts in regional wind and wave climate, although large uncertainties in change metrics over short timescales may occlude clear results.

The rapid loss of sediment volume ($R_{V,\text{DoD}} \sim 8$ m^3/m/yr) in spring/summer versus slower/negligible rate of change observed in fall and winter demonstrates that the daily sea breeze-generated waves of the warm months ultimately caused the most geomorphic change in this system, rather than the infrequent wet-season storm events. This is in contrast to open-ocean sandy beach morphodynamics of the California coast, where summer accretion and winter erosion are typical (Yates et al., 2009). Our observations may be attributed to the geometry of SSFB, which provides relatively long fetch along the dominant spring/summer sea breeze direction (northwesterly) and shorter winter storm fetch (southwesterly); the importance of wind direction and system geometry has been reported by Fagherazzi and Wiberg (2009), Duvall et al. (2019), and Houttuijn Bloemendaal et al. (2023). In SSFB, this alignment of fetch and wind directions with the sea breeze can drive relatively large daily H_S values. During winter storms, the similarly large H_S values but with much lower frequency simply cannot do as much geomorphic work. It is likely that the few remaining marshlands in eastern SSFB directly exposed to bay waves are subject to the same seasonal pattern. The outsize role of summer sea breeze-driven processes has previously been linked to marsh sediment import (Lacy et al., 2020). Additionally, interannual climate in California is highly variable and some years may have many more or fewer storms in total, exacerbating or shrinking the difference between dependable spring/summer dynamism and sporadic fall/winter calm. The El Niño Southern Oscillation may lead to decadal-scale variation too, with El Niño periods producing weaker upwelling in the Eastern Pacific (Jacox et al., 2015) and thus likely a weaker sea breeze.

5.2. Marsh-Mudflat Morphodynamics

Although the intent of this study was to capture rapid marsh-edge retreat, the various methods for detecting short-term marsh-edge retreat illuminated ways by which the marsh-mudflat system may be accumulating sediment as well. All of the metrics of retreat presented in Table 2 captured rapid loss of marsh at the marsh edge, typically via landward (eastward) retreat of the marsh scarp (Figure 5c).

The expectation of marsh-scarp retreat was complicated by a number of positive R_L values across the marsh. The steep and tall marsh scarp has no particular mechanism for progradation. While it may undergo slumping—where a block of cohesive sediment slips off the face and lands near the toe of the scarp—the slump block remains exposed to wave-based impact and cannot get replaced on the marsh-edge without degradation to smaller pieces. Many small positive R_L values were well within the bounds of combined horizontal uncertainty of our DSMs (Table 1), as reflected by the ranges presented in Table 2: we found about a third of positive R_L values to be within positional uncertainty of the marsh-edge curve. Vertical uncertainty also appears to have contributed to positive R_L values: due to the sharp gradient change from steep scarp to flat marsh top, if the histogram-determined head elevation curve was drawn on the marsh platform top, just a 3% grade (observed on the marsh top near the scarp) with the 0.103 m vertical uncertainty from the September 2021 DSM could have led to a ~31 cm horizontal change in marsh-edge curve placement. While the use of a head elevation mostly below the marsh-top surface helped reduce the impact of this effect, in regions of the marsh where the scarp fell below our fixed elevation the movement of features on top of the marsh surface led to large positive but non-outlier R_L values, especially in the Fall season. Upon inspection, about 91% of positive R_L values greater than 0.30 m/yr between September and November 2021 were attributable to the bayward movement of small sand or shell hash beaches *atop* the marsh platform (Figure 7a). In the summer and spring seasons, these small perched beaches generally migrated inland (but their influence on bulk marsh metrics was obscured by the rapid edge retreat at other transects); in the winter they were virtually immobile. This suggests these marsh-top sand/shell hash beaches may be built inland during wavy periods, and "relax" bayward as the wave season tapers. When performing analysis based on the position of the marsh edge curve, researchers should be prepared to acknowledge drawbacks such as these of using specified elevations or single curves as shorelines. Further study is merited to understand with precision relative differences
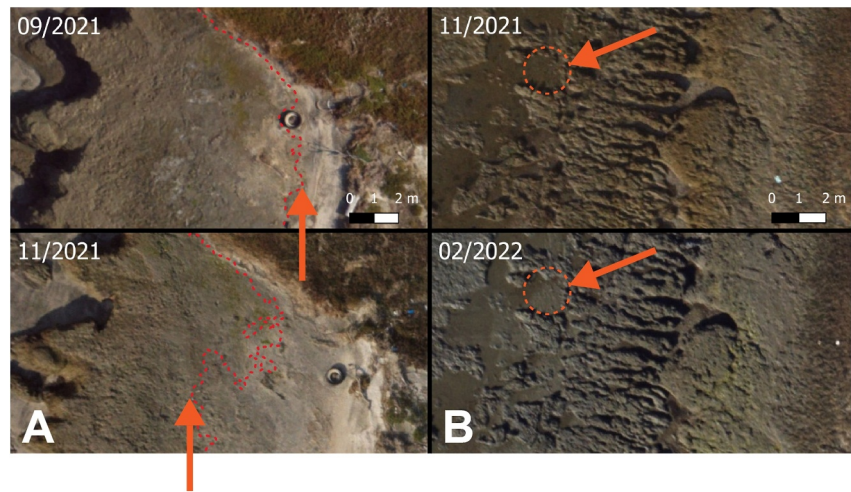
Figure 7. (a) Demonstrates a region of positive linear retreat (i.e., progradational) values, where a marsh-top beach has prograded between surveys, serving as an example of the risks in using a fixed-elevation marsh-edge curve across an variety of marsh-top landforms. (b) Points to what can be observed from orthomosaic imagery in a region of sediment accretion, a high-texture region of the fronting mudflats with positive volumetric change (i.e., accretion).

of various techniques for marsh-edge delineation, and while we discuss some in Section 5.4, we found our volumetric approach within a dynamic mudflat-marsh edge to be illuminating of surface landform dynamics.

R_L and R_V metrics reflected similarly strong seasonal patterns, but the volume-based techniques included much more than scarp-failure retreat, registering accumulation of sediment in the fall and winter seasons. This presumed import fell within the region between the head and toe curves (green lines in Figure 5b), leading to positive R_V values from accretion in the transition region just offshore of the scarp. Close inspection of the DoDs revealed that there was vertical erosion (i.e., elevation lowering) of this transitional region in the spring and summer, varying in value but with change as much as -8 cm over a season, contributing to the strongly negative volume change values. During the fall and winter seasons, there was small vertical accretion evident, up to $+5$ cm over a season. In the fall/winter, broad mudflat regions of accretion mixed with low rates of marsh-edge retreat led to weakly positive $R_{V,\text{DoD}}$ and median $R_{V,\text{tsect}}$ values over the entire marsh. The very large positive individual $R_{V,\text{tsect}}$ values, particularly in the fall season, came mostly from two portions of the marsh with accretion evident over wider regions in medium-slope (3%–5%) features directly bayward of the scarp (Figure 7b highlights where this was evident—albeit subtly—in the orthomosaic imagery). These features appeared as high-texture regions of cohesive block-like features, where the highly textured bed might lead to slower flow, sediment settling, and ultimately sediment retention. Our findings support the necessity of considering mudflats and marshes as intertwined sedimentary and geomorphic systems, ala Donatelli et al. (2018); Bouma et al. (2016), and highlight how storage of sediment in geomorphic features may occur at a seasonal timescale. The marsh-mudflat system may be importing and exporting simultaneously, and the components may serve as different stocks within a unified sediment budget.

Outside of these particular regions of marsh-mudflat system accretion, we found it difficult to attribute cause to the spatial heterogeneity of marsh-edge retreat rates. We observed no particular transect-level relationships between R_L or $R_{V,\text{tsect}}$ values and transect maximum slope or azimuth in any study period. The relatively low rate of retreat at the extreme north end of the marsh may be attributable to wave protection by the north-south running breakwater (visible in the top-left corner of Figure 5a). The larger range in retreat values during seasons with higher mean wave power values suggests that wave impact encourages marsh morphologic change, though the exact mechanism may not be tightly linked, from wave variability at the shoreline or cumulative/time-lagged wave effects as mentioned in Section 5.1. The difficulties in ascribing process-based description to small-scale heterogeneity in marsh-edge retreat have been well-documented by Houttuijn Bloemendaal et al. (2021), who found no clarity in the control effects of shoreline geomorphic "type" or four geotechnical properties, although yet understudied are the potential effects of burrowing benthic biota on retreat rates. Despite our observed seasonal signal, the exact mechanistic controls on small-spatiotemporal marsh change remain an amalgamation of other

parameters. And while the complexity in shape of this shoreline is evident (e.g., in Figure 5B), we found no clear connection between segment fractal dimension and retreat rate. Comparisons of fractal dimension against prior studies (Leonardi, Defne, et al., 2016) are limited by our unprecedented 5 cm DSM resolution.

5.3. Context of Retreat

On century-millennial timescales, marshes are transient landforms (Fagherazzi, 2013), responding to conditions of sediment supply and sea level, moving upland with sufficient sediment and space, or vanishing by retreat or drowning (K. Thorne et al., 2018). Work by Watson and Byrne (2013) found that SSFB marshes were expanding in the 1300–1800s. The development of the San Francisco Bay Area and its upland systems from the mid-1800s onwards, including re-routing, channelization, and damming of numerous channels has gradually reduced the total volume of sediment delivered to the bay (Wright & Schoellhamer, 2004), impacting the possible trajectories for marsh development. In recent decades, however, SSFB was found to be net accretive as a sub-embayment (Jaffe & Foxgrover, 2006). The majority of suspended sediment is delivered to the bay during storm events in the wet season (Barnard et al., 2013).

While previous studies have found both accretion and erosion at bay-marsh edges in San Francisco Bay (as mentioned in Section 1), annualized marsh-edge retreat at our site is rapid (<-2 m/yr) for San Francisco Bay. This may be in-part due to one of the longest possible fetch distances in the region from daily sea breeze winds from the NW incident on WTMS (Figure 4), relative to other erosional marshes with different orientations toward open bay waters. The effect of strong diurnal wind patterns and down-fetch orientation of flats in the southeastern reach of the embayment was previously linked to an erosional regime in the intertidal flats by Jones and Jaffe (2013).

Satellite imagery from the 1980s suggest that the marsh platform at WTMS has been retreating from its bay interface at least since then. Alameda Creek, one of the largest fluvial systems of SSFB (Stanford et al., 2013), discharged southwards through the middle of WTMS until it was rerouted further south around the middle of the 20th century. The former creek bed was straightened into a leveed east-west running flood-control channel just north of WTMS called "Old Alameda Creek" (Figure 1). It is likely that these engineering changes reduced the load of sediment through and proximate to WTMS. Whatever sediment is available for accretion may be most efficiently captured in vegetated regions: the lack of vegetation near the marsh-mudflat transition at WTMS may hinder the capacity for wave attenuation (Foster-Martinez et al., 2018) and thus sediment import for long-term accretion. WTMS is relatively "high-energy" in its exposure to surface waves, which is a factor in preventing its bay boundary from prograding. A scarped type of marsh-edge morphology is inherently unstable due to mass failure at the scarp (Bendoni et al., 2016), a "non-equilibrium" landscape in the words of Fagherazzi et al. (2013). While marshes with sharp scarp boundaries are also found in North San Francisco Bay, both prograding and retreating (Beagle et al., 2015), whether a marsh is prograding or retreating depends on the fate of eroded sediment: if it remains local, staying near the marsh toe and building on the mudflat elevation, it may allow vegetation growth further offshore, as presented in a conceptual model by Beagle et al. (2015). We observed some small patches of measurable accretion near the marsh boundary in fall/winter (mentioned in Section 5.2), but at the annual scale their magnitudes were outweighed by the volumetric removal of sediment at the marsh edge and mudflat erosion in the spring/summer.

Even if the eroded marsh-edge sediment does not remain by the marsh toe, it may still stay within the marsh system. Edge erosion has been considered a driving factor behind vertical marsh accretion (Duvall et al., 2019; Fagherazzi et al., 2013; Mariotti & Carr, 2014). Sediment may be effectively "recycled" from the eroding edge and then deposited on the marsh top via suspension on high tides, though this pathway is dependent on wind and wave conditions (Duvall et al., 2019). Further study may reveal if this is true for a high marsh site like WTMS, where tidal inundations are brief and typically occur only during spring tides. Because of the levee constraints around WTMS, erosion of the marsh edge nonetheless leads to a loss in total marsh area. This is likely part of a negative feedback loop of sediment trapping across the marsh system or even region (Donatelli et al., 2018). As mentioned in Section 5.1, it is likely that the other marshes exposed to bay waves in this southeastern portion of San Francisco Bay are subject to similar processes. However, the variety in orientations, fetches, sediment resources, and vegetation communities in other marshlands of San Francisco Bay means that other sites may have their dynamics dominated by other processes; marsh collapse can occur due to edge erosion (Fagherazzi et al., 2013) or drowning (K. Thorne et al., 2018; Stralberg et al., 2011).

5.4. Drawing the Marsh-Edge Boundary

Our approach for delineating the boundary between bay and marsh was motivated by the need for a method that could be made automatic with the data available and relevant to the geomorphic goals of this project. Generally, a vegetative boundary may serve better as an edge of where a marsh—as a vegetative community rather than a landform—begins and ends. However, at WTMS, the pronounced elevation difference between fronting mudflats and high-marsh platform were a defining feature of the mudflat-to-marsh *geomorphic* transition. We explored use of satellite-product NDVI thresholds as marsh-edge boundaries (ala Tuxen et al. (2008)), but found poor NDVI differentiation between mudflat and sediment-coated intertidal vegetation. Additionally, relying on satellite-based products was limited given their uncontrolled capture time; Sun et al. (2018), exploring satellite NDVI-based marsh classification, found it only feasible to identify land cover types every few years, making difficult our study goals to capture sub-annual retreat. Using our orthomosaic RGB images, we also found VARI (Visible Atmospherically Resistant Index, a substitute for NDVI using only R, G, and B reflectance bands) performed poorly in delineating a vegetation edge. Using these indexes required time-consuming cleaning and interpretation of marsh-edge boundaries, which we sought to avoid.

The approach presented here of using our DSMs toward an elevation histogram/hypsometric curve-based method ultimately serves as a geomorphically meaningful and semi-automatable technique to delineate the marsh edge, relative to manual drawing of the boundary from aerial imagery as done by Leonardi, Ganju, and Fagherazzi (2016), Carkin et al. (2020), and Beagle et al. (2015). However, expert judgment is still necessary to navigate interpretation of the contour curves drawn as the "marsh edge," even geomorphically, varies in elevation across any giveen system; without caution, the region bounded by our fixed-elevation curves may unintentionally include or exclude particular features leading to misinterpretation of calculated change. Additionally, because the boundary is drawn at an elevation contour, its location is sensitive to both vertical and horizontal uncertainties of a given DSM. When the head curve elevation we used fell on the low-gradient marsh-top surface rather than the high-gradient scarp edge, it included some regions not intended for study: these issues and more are discussed in Section 5.2. In a system with ramplike morphology and no clear elevation distinction between marsh and mudflat, this histogram-based technique is likely to fail to identify a geomorphically relevant boundary elevation value. Another technique for edge delineation when DSMs are available is identification of the maximum slope, as used in Hogan et al. (2021) and Farris et al. (2019). We found this technique challenging to implement in our heterogeneous system where some portions of shoreline were notably steeper than others, some portions of the marsh had multiple steep scarps between terraces, and small clump features could be difficult to differentiate from the main scarp edge in their slope.

Our calculated head contour position ultimately agreed well with what one might draw by eye and was also very close to the 2.14 m (NAVD88) mean higher-high water elevation of SSFB as measured at the Redwood City NOAA station (Figure 1b), a common elevation for use in beach shoreline change analysis. We compared the curve drawn by this technique to a marsh edge boundary drawn by visual inspection of an orthomosaic image from the May 2022 survey. We found the automatically drawn fixed-elevation curve was within 0.5 m of the hand-drawn curve over 95% of the marsh length. The marsh edge as drawn by hand fell at an average elevation of 1.85 m (NAVD88), with 0.21 m standard deviation; thus our fixed-elevation contour was typically positioned further inland.

5.5. Comparison With Wave Power-Marsh Retreat Relations

Numerous previous studies have established relationships between incident wave power and linear or volumetric marsh retreat rates (Bendoni et al., 2016; Cadigan et al., 2023; Marani et al., 2011; McLoughlin et al., 2015; Mel et al., 2022; Priestas et al., 2015; Schwimmer, 2001). These relationships have typically been linear or weakly power-law (exponent of 1.1 in Schwimmer (2001)), although Houttuijn Bloemendaal et al. (2023) highlight that power-law relationships may often be more appropriate given common distributions of retreat rates and wave power values, contrary to the scaling argument by Marani et al. (2011). Relationships have been populated using a variety of methods (some summarized in Cadigan et al. (2023)). For wave metrics, some studies use parameterized formulas ala Breugem and Holthuijsen (2007) while others used modeled waves; for edge retreat rates, many used erosion pins inserted horizontally into the marsh scarp, whereas others surveyed the marsh-edge or drew it from aerial imagery. Generally, volumetric retreat rates have been calculated by multiplication of linear retreat rates by a scarp height, $R_V = R_L * h$.
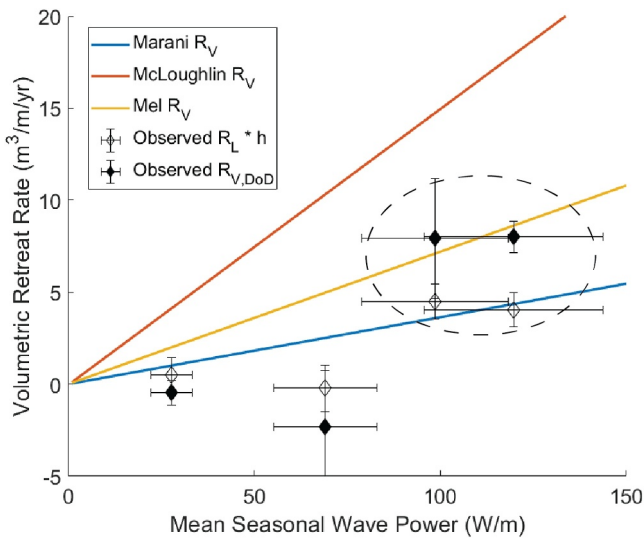
Figure 8. Relationships between mean incident wave power (P_W) and volumetric retreat rates (R_V) by Marani et al. (2011) ($R_V = 0.0364 * P_W$), McLoughlin et al. (2015) ($R_V = 0.15 * P_W - 0.05$), and Mel et al. (2022) ($R_V = 0.072 * P_W$). Our study linear volumetric retreat rates by linear retreat (R_L multiplied by scarp height $h \approx 1.8$ m) and volumetric difference ($R_{V,\text{DoD}}$) values are presented as diamonds, with 20% error in wave power and error values from Table 2 on volumetric retreat. The dashed-line circle represents the approximate span of possible data established by our observed two seasons of rapid retreat.

Data from our study year—even accretional seasons, which complicate the narrative—are presented alongside the models from Marani et al. (2011); McLoughlin et al. (2015); Mel et al. (2022) in Figure 8 (The relationship from Priestas et al. (2015) agrees closely with McLoughlin et al. (2015), and the model in Schwimmer (2001) underpredicted retreat rates at WTMS by an order of magnitude, thus they are excluded). We included $R_V = R_L * h$ using data from our study as well, for methodological comparison. To do this we used 1.8 m as h, with uncertainty on h determined as the summed-in-quadrature standard deviations of elevations of hand-drawn head and toe curves from the May 2022 survey, as previously mentioned in Section 3.2 −0.21 and 0.08 m, respectively. Our study year and the erosional seasons broadly fell within the range established by these relationships, but with two seasons registering accretion, direct assessment of compatibility is limited. However, attention should be drawn to the spread of R_V values that emerged out of different techniques for quantification. Our observed volumetric retreat rate via DSM differencing $R_{V,\text{DoD}}$ was nearly a factor of two greater than $R_V = R_L * h$ values from our own data. Although high-resolution DSMs allowed for an unprecedented level of detail in marsh-edge study, the uncertainties that followed from DSM differencing using SfM-derived data were large on seasonal timescales, even for a rapidly eroding marsh edge.

Methodological variability also lurks in the wave power metric: use of a parameterized wave model—i.e. those from Breugem and Holthuijsen (2007) —may produce wave metrics that do not represent the cumulative impact of calm and wavy periods, and they may not capture specific energy spectrum transformations that waves undergo as they travel across mudflats and into marsh boundaries. Furthermore, lack of specification on exact location of wave power calculations can lead to wide variation: the wave power metrics included in Table 2 and Figure 8 are from nearly 2 km offshore of WTMS, at a subtidal station where observational validation was straightforward; we found a typical 20% reduction in modeled H_S and thus about 64% reduction in modeled wave power between our sensor location and the SWAN grid cell most adjacent to the marsh scarp. Even closer to the marsh boundary, Tonelli et al. (2010) found upwards of 25% reduction in wave thrust as waves broke over the lip of a terrace feature in front of a marsh scarp. Additionally, we found mean seasonal wave power values to be about 10% less if we did not restrict analysis to time periods when water levels were between toe and head elevations. While wave power-retreat relationships are already largely system-specific (Houttuijn Bloemendaal et al., 2023), without high specificity around the exact methods for the production of wave statistics and marsh-edge retreat metrics, it remains very difficult to compare relationships between systems. Caution should be used in applying relationships without full awareness of the site nature and methods used to produce both P_w and R_V metrics.

Our study begins to illustrate how wave power and volumetric change of the combined mudflat-marsh system are related, but that not all of this change may be expressed purely as retreat of a marsh-scarp edge. A short time period between surveys raises the possibility of marsh-edge morphologic change falling under the threshold of confident quantification, deteriorating relationships between the wave power and retreat rate. In contexts with strong seasonal patterns in climatology—like California's Mediterranean climate—the months necessary between surveys to capture measurable geomorphic change may not be constant. Additionally, the role of the strong daily sea breeze defies expectations set by the frequency-magnitude storm event-based framework explored by Leonardi, Ganju, and Fagherazzi (2016) and Houttuijn Bloemendaal et al. (2023). While one can expect seasonal patterns in retreat based on average wave energy, we support Houttuijn Bloemendaal et al. (2021); Mel et al. (2022) in considering mass failure at the marsh edge as a highly location-specific process, and difficult to predict in purely mechanistic terms.

6. Conclusion

We documented rapid annualized erosion at a marsh boundary in SSFB. When performed on annual timescales, measurements of marsh-edge retreat aggregate marsh-edge collapse over seasons which might have very different wave climates. We found that in the Mediterranean climate of the San Francisco Bay Area, spring/summer

seasons dominated the annual-scale marsh-edge erosion due to strong daily onshore winds and large daily wind waves. This contrasted with fall/winter seasons characterized by calm waters punctuated by storms, which drove negligible marsh-scarp retreat. However, by using digital surface models to monitor the entire marsh-mudflat system, we found that the fall and winter seasons included accretion of sediment in the transitional toe/mudflat region between the bay and the marsh edge. Retreat rates of the marsh edge were heterogeneous at our field site within any given season but were more homogeneous over the study year and in decadal-scale analysis; together this suggests that many marsh scarp failure events which are difficult to predict on short timescales (up to seasons) can ultimately drive relatively uniform annual-scale marsh retreat at a site. Our study encourages considering evolution of mudflats and marshes as coupled sediment stocks, and addressing seasonal differences in wind and wave fields when aggregating marsh retreat statistics. When DSM data are available, our technique for delineating the geomorphic marsh-edge boundary using simple calculations is more replicable than previous studies which have often relied on human interpretation of images, extensive field mapping work, or the assumed efficacy of a nearby tidal datum. We additionally note that care should be exercised when comparing wave power-marsh retreat relationships between sites and studies, for biogeophysical reasons as well as methodological ones. Season-length intervals between surveys to quantify volumetric change challenged the levels of certainty incurred by differencing photogrammetry-derived digital surface models of the dynamic marsh environment but proved useful in quantifying season-scale change. This work may help anticipate marsh loss and inform effective monitoring, management, and restoration strategies of marshlands, introducing the idea of seasonal cycles in retreat patterns.

Data Availability Statement

Data used in this study have been referenced in the text where appropriate. The five digital surface models to study marsh retreat and volumetric change over the study year are available in the data release Logan et al. (2023). For the same purposes on longer timescales, the 2004 lidar data via Foxgrover and Jaffe (2005), the 2010 lidar data via OCM Partners (2023), and the 2019 lidar data in a DataDryad repository via WinklerPrins (2023). Observed in situ hydrodynamic data are available in Ferreira et al. (2023), and wave model input/output in WinklerPrins and Stevens (2024). Properties of the sediment and vegetation at the site, only briefly used in this study, are available in K. M. Thorne and Bristow (2023). The Digital Shoreline Analysis System software v5.1, which was used for linear retreat analysis and transect-drawing, is accessible via Himmelstoss et al. (2021) and https://code.usgs.gov/cch/dsas. For this study, DSAS was run using ESRI Arcmap v10.8.2 software https://desktop.arcgis.com/en/arcmap/index.html.

References

Anderson, S. W. (2019). Uncertainty in quantitative analyses of topographic change: Error propagation and the role of thresholding. *Earth Surface Processes and Landforms*, *44*(5), 1015–1033. https://doi.org/10.1002/esp.4551

Barnard, P. L., Schoellhamer, D. H., Jaffe, B. E., & McKee, L. J. (2013). Sediment transport in the San Francisco Bay coastal system: An overview. *Marine Geology*, *345*, 3–17. https://doi.org/10.1016/j.margeo.2013.04.005

Battjes, J. A., & Janssen, J. P. F. M. (1978). Energy loss and set-up due to breaking of random waves. In *Coastal engineering 1978* (pp. 569–587). American Society of Civil Engineers. https://doi.org/10.1061/9780872621909.034

Beagle, J., Salomon, M., Grossinger, R., Baumgarten, S., & Askevold, R. (2015). *Shifting shores: Marsh expansion and retreat in San Pablo Bay. (Tech. Rep. No. SFEI-ASC 751)*. San Francisco Estuary Institute. Retrieved from https://www.sfei.org/documents/shifting-shores-marsh-expansion-and-retreat-san-pablo-bay

Bendoni, M., Mel, R., Solari, L., Lanzoni, S., Francalanci, S., & Oumeraci, H. (2016). Insights into lateral marsh retreat mechanism through localized field measurements. *Water Resources Research*, *52*(2), 1446–1464. https://doi.org/10.1002/2015WR017966

Bouma, T. J., Van Belzen, J., Balke, T., Van Dalen, J., Klaassen, P., Hartog, A. M., et al. (2016). Short-term mudflat dynamics drive long-term cyclic salt marsh dynamics: Lateral salt marsh dynamics. *Limnology & Oceanography*, *61*(6), 2261–2275. https://doi.org/10.1002/lno.10374

Breugem, W. A., & Holthuijsen, L. H. (2007). Generalized shallow water wave growth from Lake George. *Journal of Waterway, Port, Coastal, and Ocean Engineering*, *133*(3), 173–182. https://doi.org/10.1061/(ASCE)0733-950X(2007)133:3(173)

Buffington, K. J., Dugger, B. D., Thorne, K. M., & Takekawa, J. Y. (2016). Statistical correction of lidar-derived digital elevation models with multispectral airborne imagery in tidal marshes. *Remote Sensing of Environment*, *186*, 616–625. https://doi.org/10.1016/j.rse.2016.09.020

Cadigan, J. A., Jafari, N. H., Wang, N., Chen, Q., Zhu, L., Harris, B. D., & Ding, Y. (2023). Near-continuous monitoring of a coastal salt marsh margin: Implications for predicting marsh edge erosion. *Earth Surface Processes and Landforms*, *48*(7), 1362–1373. https://doi.org/10.1002/esp.5554

Callaway, J. C., Borgnis, E. L., Turner, R. E., & Milan, C. S. (2012). Carbon sequestration and sediment accretion in San Francisco Bay tidal wetlands. *Estuaries and Coasts*, *35*(5), 1163–1181. https://doi.org/10.1007/s12237-012-9508-9

Campbell, A. D., Fatoyinbo, L., Goldberg, L., & Lagomasino, D. (2022). Global hotspots of salt marsh change and carbon emissions. *Nature*, *612*(7941), 701–706. https://doi.org/10.1038/s41586-022-05355-z

Carkin, B. A., Kayen, R. E., & Wong, F. L. (2020). *Shoreline retreat of the corte Madera marshes, 1853 to 2016, Marin County, California (Open-File Report)*. U.S. Geological Survey.

Collins, J. I. (1972). Prediction of shallow-water spectra. *Journal of Geophysical Research*, *77*(15), 2693–2707. https://doi.org/10.1029/JC077i015p02693

Conomos, T. J., Smith, R. E., & Gartner, J. W. (1985). Environmental setting of San Francisco Bay. *Hydrobiologia*, *129*, 1–12. https://doi.org/10.1007/BF00048684

Donatelli, C., Ganju, N. K., Zhang, X., Fagherazzi, S., & Leonardi, N. (2018). Salt marsh loss affects tides and the sediment budget in shallow bays. *Journal of Geophysical Research: Earth Surface*, *123*(10), 2647–2662. https://doi.org/10.1029/2018JF004617

Duvall, M. S., Wiberg, P. L., & Kirwan, M. L. (2019). Controls on sediment suspension, flux, and marsh deposition near a bay-marsh boundary. *Estuaries and Coasts*, *42*(2), 403–424. https://doi.org/10.1007/s12237-018-0478-4

Fagherazzi, S. (2013). The ephemeral life of a salt marsh. *Geology*, *41*(8), 943–944. https://doi.org/10.1130/focus082013.1

Fagherazzi, S., Mariotti, G., Wiberg, P., & McGlathery, K. (2013). Marsh collapse does not require sea level rise. *Oceanography*, *26*(3), 70–77. https://doi.org/10.5670/oceanog.2013.47

Fagherazzi, S., & Wiberg, P. L. (2009). Importance of wind conditions, fetch, and water levels on wave-generated shear stresses in shallow intertidal basins. *Journal of Geophysical Research*, *114*(F3), F03022. https://doi.org/10.1029/2008JF001139

Farris, A. S., Defne, Z., & Ganju, N. K. (2019). Identifying salt marsh shorelines from remotely sensed elevation data and imagery. *Remote Sensing*, *11*(15), 1795. https://doi.org/10.3390/rs11151795

Ferreira, J. C. T., Lacy, J. R., Mcgill, S. C., WinklerPrins, L. T., Nowacki, D. J., Stevens, A. W., & Tan, A. C. (2023). Hydrodynamic and sediment transport data from Whale's Tail marsh and adjacent waters in South San Francisco Bay, California 2021–2022 [Dataset]. *U.S. Geological Survey*. https://doi.org/10.5066/P972R6AW

Foster-Martinez, M., Lacy, J., Ferner, M., & Variano, E. (2018). Wave attenuation across a tidal marsh in San Francisco Bay. *Coastal Engineering*, *136*, 26–40. https://doi.org/10.1016/j.coastaleng.2018.02.001

Foxgrover, A. C., & Jaffe, B. E. (2005). *South San Francisco Bay 2004 topographic lidar survey: Data overview and preliminary quality assessment (Open-File Report No. 2005-1284)*. U.S. Geological Survey. Retrieved from http://pubs.usgs.gov/of/2005/1284

Gray, P. C., Ridge, J. T., Poulin, S. K., Seymour, A. C., Schwantes, A. M., Swenson, J. J., & Johnston, D. W. (2018). Integrating drone imagery into high resolution satellite remote sensing assessments of estuarine environments. *Remote Sensing*, *10*(8), 1257. https://doi.org/10.3390/rs10081257

Himmelstoss, E., Henderson, R., Kratzmann, M., & Farris, A. (2021). *Digital shoreline analysis system (DSAS) version 5.1 user guide* (Open-File Report No. 2021-1091). U.S. Geological Survey. https://doi.org/10.3133/ofr20211091

Hogan, S., Wiberg, P., & Reidenbach, M. (2021). Utilizing airborne LiDAR data to quantify marsh edge morphology and the role of oyster reefs in mitigating marsh erosion. *Marine Ecology Progress Series*, *669*, 17–31. https://doi.org/10.3354/meps13728

Houttuijn Bloemendaal, L. J., FitzGerald, D. M., Hughes, Z. J., Novak, A. B., & Georgiou, I. Y. (2023). Reevaluating the wave power-salt marsh retreat relationship. *Scientific Reports*, *13*(1), 2884. https://doi.org/10.1038/s41598-023-30042-y

Houttuijn Bloemendaal, L. J., FitzGerald, D. M., Hughes, Z. J., Novak, A. B., & Phippen, P. (2021). What controls marsh edge erosion? *Geomorphology*, *386*, 107745. https://doi.org/10.1016/j.geomorph.2021.107745

Jacox, M. G., Fiechter, J., Moore, A. M., & Edwards, C. A. (2015). ENSO and the California Current coastal upwelling response. *Journal of Geophysical Research: Oceans*, *120*(3), 1691–1702. https://doi.org/10.1002/2014JC010650

Jaffe, B., & Foxgrover, A. (2006). *Sediment deposition and erosion in South San Francisco Bay, California from 1956 to 2005 (Open-File Report No. 2006-1287)*. U.S. Geological Survey.

Jones, C. A., & Jaffe, B. E. (2013). Influence of history and environment on the sediment dynamics of intertidal flats. *Marine Geology*, *345*, 294–303. https://doi.org/10.1016/j.margeo.2013.05.011

King, A. (2019). *Wind over San Francsico bay and the Sacramento-San Joaquin river Delta: Forcing for hydrodynamic models (Tech. Rep.)*. San Francisco Estuary Institute. Retrieved from https://www.sfei.org/documents/SFEI-Winds-Technical-Report

Lacy, J. R., Foster-Martinez, M. R., Allen, R. M., Ferner, M. C., & Callaway, J. C. (2020). Seasonal variation in sediment delivery across the bay-marsh interface of an estuarine salt marsh. *Journal of Geophysical Research: Oceans*, *125*(1). https://doi.org/10.1029/2019JC015268

Leonardi, N., Defne, Z., Ganju, N. K., & Fagherazzi, S. (2016a). Salt marsh erosion rates and boundary features in a shallow Bay: Indicators Salt Marsh Erosion New Jersey. *Journal of Geophysical Research: Earth Surface*, *121*(10), 1861–1875. https://doi.org/10.1002/2016JF003975

Leonardi, N., & Fagherazzi, S. (2014). How waves shape salt marshes. *Geology*, *42*(10), 887–890. https://doi.org/10.1130/G35751.1

Leonardi, N., & Fagherazzi, S. (2015). Effect of local variability in erosional resistance on large-scale morphodynamic response of salt marshes to wind waves and extreme events: Resistance Variability Affects Marsh. *Geophysical Research Letters*, *42*(14), 5872–5879. https://doi.org/10.1002/2015GL064730

Leonardi, N., Ganju, N. K., & Fagherazzi, S. (2016b). A linear relationship between wave power and erosion determines salt-marsh resilience to violent storms and hurricanes. *Proceedings of the National Academy of Sciences*, *113*(1), 64–68. https://doi.org/10.1073/pnas.1510095112

Logan, J., Winklerprins, L. T., & Lacy, J. R. (2023). Structure-from-motion derived orthomosaic imagery and digital surface models (DSMs) from the intertidal region at Whale's Tail Marsh, South San Francisco Bay [Dataset]. *U.S. Geological Survey*. https://doi.org/10.5066/P9L9R2VS

Madsen, O. S. (1995). Spectral wave-current bottom boundary layer flows. In *Coastal engineering 1994* (pp. 384–398). American Society of Civil Engineers. https://doi.org/10.1061/9780784400890.030

Marani, M., D'Alpaos, A., Lanzoni, S., & Santalucia, M. (2011). Understanding and predicting wave erosion of marsh edges. *Geophysical Research Letters*, *38*(21), L21401. https://doi.org/10.1029/2011gl048995

Mariotti, G., & Carr, J. (2014). Dual role of salt marsh retreat: Long-term loss and short-term resilience. *Water Resources Research*, *50*(4), 2963–2974. https://doi.org/10.1002/2013WR014676

McLoughlin, S. M., Wiberg, P. L., Safak, I., & McGlathery, K. J. (2015). Rates and forcing of marsh edge erosion in a shallow coastal bay. *Estuaries and Coasts*, *38*(2), 620–638. https://doi.org/10.1007/s12237-014-9841-2

Mel, R. A., Bendoni, M., & Steffinlongo, D. (2022). Salt-marsh retreat on different time scales: Issues and prospects from a 5-year monitoring campaign in the Venice Lagoon. *Earth Surface Processes and Landforms*, *47*(8)(8), 1989–2005. https://doi.org/10.1002/esp.5359

OCM Partners. (2023). 2010 U.S. Geological survey (USGS) topographic LiDAR: San Francisco Bay [Dataset]. https://www.fisheries.noaa.gov/inport/item/50115

Over, J.-S., Ritchie, A., Kranenburg, C., Brown, J., Buscombe, D., Noble, T., et al. (2021). *Processing coastal imagery with agisoft metashape professional edition, version 1.6–structure from motion workflow documentation (Open-File Report No. 2021-1039)*. U.S. Geological Survey.

Pinton, D., Canestrelli, A., Wilkinson, B., Ifju, P., & Ortega, A. (2020). A new algorithm for estimating ground elevation and vegetation characteristics in coastal salt marshes from high-resolution UAV-based LiDAR point clouds. *Earth Surface Processes and Landforms*, *45*(14), 3687–3701. https://doi.org/10.1002/esp.4992

Priestas, A., Mariotti, G., Leonardi, N., & Fagherazzi, S. (2015). Coupled wave energy and erosion dynamics along a salt marsh boundary, Hog Island bay, Virginia, USA. *Journal of Marine Science and Engineering*, *3*(3), 1041–1065. https://doi.org/10.3390/jmse3031041

Rolstad, C., Haug, T., & Denby, B. (2009). Spatially integrated geodetic glacier mass balance and its uncertainty based on geostatistical analysis: Application to the western Svartisen ice cap, Norway. *Journal of Glaciology*, *55*(192), 666–680. https://doi.org/10.3189/002214309789470950

Ruggiero, P., Kratzmann, M. G., Himmelstoss, E. A., Reid, D., Allan, J., & Kaminsky, G. (2013). *National assessment of shoreline change: Historical shoreline change along the Pacific northwest coast (Open-File Report No. 2012-1007)*. U.S. Geological Survey. https://doi.org/10.3133/ofr20121007

Schwimmer, R. (2001). Rates and Processes of Marsh Shoreline Erosion in Rehoboth Bay, Delaware, U.S.A. *Journal of Coastal Research*, *17*(3), 13.

Stanford, B., Grossinger, R., Beagle, J., Askevold, R., Leidy, R., Beller, E., et al. (2013). Alameda Creek Watershed Historical Ecology Study. *San Francisco Estuary Institute*. Retrieved from https://www.sfei.org/documents/alameda-creek-watershed-historical-ecology-study

Stralberg, D., Brennan, M., Callaway, J. C., Wood, J. K., Schile, L. M., Jongsomjit, D., et al. (2011). Evaluating Tidal Marsh Sustainability in the Face of Sea-Level Rise: A Hybrid Modeling Approach Applied to San Francisco Bay. *PLoS One*, *6*(11), e27388. https://doi.org/10.1371/journal.pone.0027388

Sun, C., Fagherazzi, S., & Liu, Y. (2018). Classification mapping of salt marsh vegetation by flexible monthly NDVI time-series using Landsat imagery. *Estuarine, Coastal and Shelf Science*, *213*, 61–80. https://doi.org/10.1016/j.ecss.2018.08.007

Swain, D. L., Langenbrunner, B., Neelin, J. D., & Hall, A. (2018). Increasing precipitation volatility in twenty-first-century California. *Nature Climate Change*, *8*(5), 427–433. https://doi.org/10.1038/s41558-018-0140-y

Talke, S., & Stacey, M. (2003). The influence of oceanic swell on flows over an estuarine intertidal mudflat in San Francisco Bay. *Estuarine, Coastal and Shelf Science*, *58*(3), 541–554. https://doi.org/10.1016/S0272-7714(03)00132-X

Thorne, K., MacDonald, G., Guntenspergen, G., Ambrose, R., Buffington, K., Dugger, B., et al. (2018). U.S. Pacific coastal wetland resilience and vulnerability to sea-level rise. *Science Advances*, *4*(2), eaao3270. https://doi.org/10.1126/sciadv.aao3270

Thorne, K. M., & Bristow, M. L. (2023). Sediment deposition and accretion data from a tidal salt marsh in South San Francisco Bay, California 2021-2022. *U.S. Geological Survey*. https://doi.org/10.5066/P9YBBXIZ

Tonelli, M., Fagherazzi, S., & Petti, M. (2010). Modeling wave impact on salt marsh boundaries. *Journal of Geophysical Research*, *115*(C9), C09028. https://doi.org/10.1029/2009JC006026

Torio, D. D., & Chmura, G. L. (2013). Assessing Coastal Squeeze of Tidal Wetlands. *Journal of Coastal Research*, *290*, 1049–1061. https://doi.org/10.2112/JCOASTRES-D-12-00162.1

Tuxen, K. A., Schile, L. M., Kelly, M., & Siegel, S. W. (2008). Vegetation Colonization in a Restoring Tidal Marsh: A Remote Sensing Approach. *Restoration Ecology*, *16*(2), 313–323. https://doi.org/10.1111/j.1526-100X.2007.00313.x

Van Der Westhuysen, A. J., Zijlema, M., & Battjes, J. A. (2007). Nonlinear saturation-based whitecapping dissipation in SWAN for deep and shallow water. *Coastal Engineering*, *54*(2), 151–170. https://doi.org/10.1016/j.coastaleng.2006.08.006

Watson, E. B., & Byrne, R. (2013). Late Holocene Marsh Expansion in Southern San Francisco Bay, California. *Estuaries and Coasts*, *36*(3), 643–653. https://doi.org/10.1007/s12237-013-9598-z

Wiberg, P. L., & Sherwood, C. R. (2008). Calculating wave-generated bottom orbital velocities from surface-wave parameters. *Computers and Geosciences*, *34*(10), 1243–1262. https://doi.org/10.1016/j.cageo.2008.02.010

Williams, P., & Faber, P. (2001). Salt Marsh Restoration Experience in San Francisco Bay. *Journal of Coastal Research*, *27*(9), 203–211.

WinklerPrins, L. (2023). Lidar-derived digital elevation model of whale's tail marsh, San Francisco Bay, 2019 [Dataset]. *Dryad*. https://doi.org/10.6078/D1BH9Z

WinklerPrins, L., Largier, J. L., Vila-Concejo, A., Gallop, S. L., Fellowes, T. E., & Rahbani, M. (2023). Components and Tidal Modulation of the Wave Field in a Semi-enclosed Shallow Bay. *Estuaries and Coasts*, *46*(3), 645–659. https://doi.org/10.1007/s12237-022-01154-x

WinklerPrins, L., & Stevens, A. (2024). Modeled surface waves from winds in South San Francisco Bay [Dataset]. https://doi.org/10.5066/P9QH0GU5

Wright, S., & Schoellhamer, D. (2004). Trends in the Sediment Yield of the Sacramento River, California, 1957–2001. *San Francisco Estuary and Watershed Science*, *2*(2). https://doi.org/10.15447/sfews.2004v2iss2art2

Yates, M. L., Guza, R. T., & O'Reilly, W. C. (2009). Equilibrium shoreline response: Observations and modeling. *Journal of Geophysical Research*, *114*(C9), C09014. https://doi.org/10.1029/2009JC005359